Internal Simulation for Autonomous Robot Exploration of Lava Tubes

Raúl Domínguez, Sascha Arnold, Christoph Hertzberg and Arne Böckmann
German Research Center for Artificial Intelligence – Robotics Innovation Center,
Robert-Hooke-Str. 1, 28359 Bremen, Germany

Keywords: Autonomous Navigation, Robotics Simulation, Path Planning, SLAM, Exploration.

Abstract: Space Exploration stands as one of the most challenging endeavors of our time. Extraterrestrial caves in particular have been identified by the scientific community as of great interest. They could be suitable for allocating astronaut planetary stations, but little is known about them. In this paper, we describe and analyze robotic cave exploration using internal simulation and SLAM technologies and provide experimental results. The experiments were performed in a lava tube selected due to its representativeness as space analog. Expensive mission costs, communication constraints and navigational challenges in space missions demand highly developed degrees of autonomy and safety on the robots. For this reason, our solution incorporates methods for the validation of paths based on on-board, internal simulation. The methods provide the means to increase the confidence of successful executions by simulating using physics models the planned path. A highly realistic model of the robot and an on-line generated model of the environment are required. Assuming the demands of the space robotics scenario, all software runs on-board.

1 INTRODUCTION

Caves are an important cornerstone of human space exploration (Wynne, 2016). They can provide a natural shelter from radiation, extreme temperature cycles and small meteoroids, allowing the deployment of light-weight habitats and reducing the overall costs. Caves might also provide access to water ice deposits and protected underground environments that can reveal information about geological processes and potential extraterrestrial life. Lava tubes have been identified in Moon and although they have not yet been confirmed in Mars, there is significant evidence of their existence (Daga et al., 2009). In fact, many cave-like features have been identified on Mars and on Moon in the recent years.

To reduce the risks and to ensure the suitability of a cave for allocating astronauts or any other possible usage, robotic platforms can be used to generate maps and analyze the state of the tubes. When going underground, robotic systems must maintain a constant data-link to the surface, usually done by a wire (Nesnas et al., 2012), or be able to explore the cave autonomously. Although a wire link can be beneficial to reach the entrance, it will easily get entangled and limits the exploration range in the tube. In this paper we focus on the internal simulation as a key element that enables a robot equipped with a LiDAR to autonomous explore, map and find it's way back in a cave.

Figure 1: The Asguard V4 rover. A four leg-wheel hybrid robot designed for difficult outdoor environments, equipped with an embedded quad core i7 CPU, a Velodyne LiDAR, Xsens IMU and a 360 degree camera. Additionally the rover can carry payloads of up to 5 kg (e.g. a spectroscope or sampling drill) Image: Robbie Shone, ESA.

For performing the experiments and to analyse our software and hardware, we selected the lava tube *Cueva del Viento* in Icod de los Vinos (Spain). *Cueva del Viento* is the largest lava tube in Europe. It is located at the volcanic island of Tenerife, an exceptional location for planetary analog environments (Preston

Domínguez, R., Arnold, S., Hertzberg, C. and Böckmann, A.
Internal Simulation for Autonomous Robot Exploration of Lava Tubes.
DOI: 10.5220/0006860701440155
In *Proceedings of the 15th International Conference on Informatics in Control, Automation and Robotics (ICINCO 2018) - Volume 2*, pages 144-155
ISBN: 978-989-758-321-6

et al., 2012). For the exploration mission, a 240 m long section of the tube was selected which is preserved without any human modification and where the risks of collapse were very low. As platform for our experiments we utilized the Asguard V4 rover shown in Fig. 1.

The entrance to the cave is located in a cavity of the floor, with a height of around 0.5 m and a width of approximately 0.75 m. After the entrance through the small opening, follows an inclined and muddy surface. In a real mission, this first section would have to be traversed by the robot with the help of some rope or cable. In a multi-robot mission this objective could be achieved.

Nowadays, planetary robotic missions rely heavily on the operations center at earth for navigation. The paths that the robot executes are designed on earth with human experts in the loop, based on the data acquired in the previous days. This approach is safe, but makes planetary exploration very slow. Furthermore, in the case of long caves, like the one described in the experimental part, communication with earth for each path execution implies entering and leaving the cave constantly. Thus, in order to explore the cave in depth, an autonomous system which provides larger exploration ranges is preferable. The proposed solution does not require human intervention for the safe navigation and mapping of the cave.

One of the most important features of space robotic systems is safety. In order to address this issue, our solution incorporates an on-board simulator. The internal simulator enables the system to predict what the consequences of the potential path plan executions would be. The concept is based on ideas from the Simulation Cognition Theory (Hesslow, 2012). (Marques and Holland, 2009) propose a framework which includes the minimal requirements, components, a taxonomy of architectures and examples of these. The internal simulator has been previously identified as a useful approach for decision taking and path planning in space robotics in (Roßmann et al., 2014; Domínguez et al., 2015) and for planning and navigation in indoor environments (Rockel et al., 2014; Rockel et al., 2015; Chella and Macaluso, 2009).

As opposed to other works, our internal simulator runs on-board and uses a simulated environment which was generated online by the rover from its collected sensor data. To achieve this, our SLAM and our Simulator have been designed to share and work on the same environment representation using the library Envire (Hidalgo Carrió et al., 2016).

Environment representation and navigation in cave missions impose additional path planning and mapping requirements with respect to other space robotics cases. In particular, lava tubes can form 3 dimensional pathways which are not found in open areas. At this point, traditional 2 dimensional grid-based path planning algorithms become insufficient. Our environment representation, path planner and exploration components are able to represent, explore and find motion plans in such environments. This is achieved by incorporating a third dimension on the grid map and by building a bi-directional graph of connected traversable areas from it.

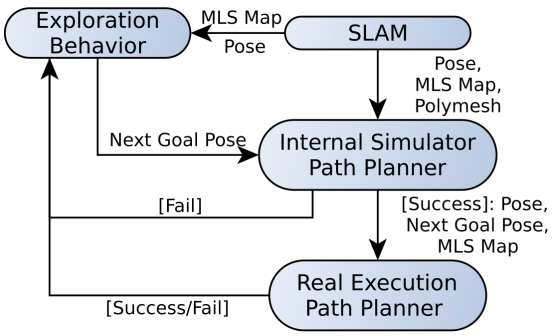

Figure 2: Approach for the Autonomous Cave Exploration: Explorer chooses a goal pose in a travesable area close to an unknown region. Internal Simulator executes the path planning on-board. If the result is successful, the planning in the real environment is executed. Feedback is given to the Explorer.

The proposed SLAM, Path Planning, Exploration and Internal Simulation methodology are presented in Section 2. The result of its evaluation with experimental cases is presented in Section 3. Conclusions are presented in Section 4 along with the next research goals.

2 METHODOLOGY

Our overall approach is shown in Fig. 2. The Exploration Behavior is in charge of selecting the next target pose based on the known Multi-Level Surface (MLS) map, the current pose and feedback from the internal simulator regarding previously attempted goal poses. SLAM is responsible for the localization and for the construction and maintenance of the Environment Representation in its different forms: MLS Maps for planning and Polymeshes for internal simulation. The Internal Simulator replicates the path planning components and its execution to identify whether the traverse to a goal pose is feasible. Finally, the Path Planner executes the motion plan in the real environment if the result of the prediction is a success.

Although the Exploration Behavior is the direct-

ing component, it highly depends on the inputs from the other modules. Thus, SLAM, Path Planning and the Internal Simulator are explained first.

2.1 SLAM

The SLAM solution used in this work is a graph SLAM approach in which odometry, LiDAR and inclination based constraints are online modeled and optimized. The state space consists of the robot poses, each associated with a 360 degree LiDAR scan and a bias state modeling the IMU to LiDAR rotation error. The LiDAR has a vertical resolution of 1.25° covering the range from -30° to 10° and a horizontal resolution of 0.18°. In order to model the inclination of the IMU and the relative transformations between the LiDAR scans together, the pose of the IMU with respect to the LiDAR needs to be calibrated. Modeling the bias allows to associate this calibration with an uncertainty and therefore avoids that the optimization becomes overconfident. In case of a low accuracy calibration it also allows refining the calibration by starting with a higher uncertainty.

In order to perform the graph optimization in real-time we reduce the amount of constraints by modeling only the result of the ICP algorithm based alignment between two LiDAR scans as a constraint. The technique relies on the Generalized-ICP (GICP) from (Segal et al., 2009). As odometry constraint we apply the wheel rotation rates and the orientation provided by the IMU to a skid-steer kinematics model of the robot. Modeling the IMU based inclination constrains the error in roll and pitch and therefore reduces the error in altitude.

Since we consider a 360 degree LiDAR scan with an acquisition time of 0.1 seconds to be a static measurement of the environment we have to convert the single measurements into the same frame. We apply interpolated odometry based transformations to each of the 64K measurements in order to convert them into the acquisition time of the first measurement. This allows us to deal with motion distortions inside a full scan resulting from fast (particularly roll/pitch) motion of the robot, due to the stiff and unstructured surfaces usually found in lava tubes.

Each state $\mathbf{x}_t \in SE(3)$ is associated with a point cloud measurement of the surrounding environment. New states are added to the graph based on the change in rotation and translation of the robot. The ICP based measurement is defined as

$$\mathbf{z}_{l,t,j} = \mathbf{C}_{x_j}^{-1}\mathbf{C}_{x_t} \boxplus \varepsilon_{l,t} \tag{1}$$

where $\mathbf{C}_{x_t}$ is the transformation matrix of the state $\mathbf{x}_t \in SE(3)$. ICP based constraints are added for each state $\mathbf{x}_t$ to the j states within the closest Euclidean distance. ε_l is a Gaussian random variable modeling the ICP measurement noise with zero mean and a covariance $\mathbf{Q}_l$. The constraint of the ICP based edges is modeled as

$$(\mathbf{z}_{l,t,j} \boxminus \mathbf{C}_{x_j}^{-1}\mathbf{C}_{x_t})^\top \mathbf{Q}_{l,t}^{-1} (\mathbf{z}_{l,t,j} \boxminus \mathbf{C}_{x_j}^{-1}\mathbf{C}_{x_t}) \tag{2}$$

where $\mathbf{z}_{l,t,j} \in SE(3)$ is the result of point cloud alignment of the ICP algorithm. The $\boxplus$ operator adds a local perturbation $\varepsilon \in \mathbb{R}^3$ to a manifold element $x \in SE(3)$: $\varepsilon \mapsto x \boxplus \varepsilon$ and $\boxminus$ is the corresponding reverse operator $\boxminus : SE(3) \times SE(3) \to \mathbb{R}^3$. For more mathematical details we refer the reader to (Hertzberg et al., 2013).

The odometry measurement is defined as

$$\mathbf{z}_{o,t} = \mathbf{C}_{x_{t-1}}^{-1}\mathbf{C}_{x_t} \boxplus \varepsilon_{o,t} \tag{3}$$

where ε_o is a Gaussian random variable modeling the odometry measurement noise with zero mean and a covariance $\mathbf{Q}_o$. Odometry based constrains are only added between successive states $\mathbf{x}_{t-1}$ to $\mathbf{x}_t$. The constraint of the odometry based edges is modeled as

$$(\mathbf{z}_{o,t} \boxminus \mathbf{C}_{x_{t-1}}^{-1}\mathbf{C}_{x_t})^\top \mathbf{Q}_{o,t}^{-1} (\mathbf{z}_{o,t} \boxminus \mathbf{C}_{x_{t-1}}^{-1}\mathbf{C}_{x_t}) \tag{4}$$

where $\mathbf{z}_{o,t} \in SE(3)$ is the measurement of the skid-steer kinematics model from $t-1$ to t.

The measurement of the inclination is defined as

$$\mathbf{z}_{h,t} = \mathbf{R}_b^{-1}\mathbf{R}_{x_t}^{-1}\hat{k} \boxplus \varepsilon_{h,t} \tag{5}$$

where $\mathbf{R}_{x_t}$ is the rotation matrix of the state $\mathbf{x}_t$, $\mathbf{R}_b$ is the rotation matrix of the bias state $\mathbf{b}$ and $\hat{k}$ is the unit vector $[0,0,1]^\top$. The bias $\mathbf{b} \in SO(3)$ describes the error in the IMU to LiDAR rotation. ε_h is a Gaussian random variable modeling the inclination measurement noise with zero mean and a covariance $\mathbf{Q}_h$. The constraint of the inclination edges is modeled as

$$(\mathbf{z}_{h,t} \boxminus \mathbf{R}_b^{-1}\mathbf{R}_{x_t}^{-1}\hat{k})^\top \mathbf{Q}_h^{-1} (\mathbf{z}_{h,t} \boxminus \mathbf{R}_b^{-1}\mathbf{R}_{x_t}^{-1}\hat{k}) \tag{6}$$

where $\mathbf{z}_{h,t} \in S^2$ is the measurement of inclination from an IMU.

The graph optimization minimizes the squared error of all constraints given all measurements $(\mathbf{z}_{l,1:t}, \mathbf{z}_{o,1:t}, \mathbf{z}_{h,1:t})$ to find the best solution for the states $\mathbf{x}_{1:t}$ and $\mathbf{b}$.

$$\arg\max_{\mathbf{x}_{1:t},\mathbf{b}} p(\mathbf{x}_{1:t}, \mathbf{b} | \mathbf{z}_{l,1:t}, \mathbf{z}_{o,1:t}, \mathbf{z}_{h,1:t}) \tag{7}$$

We use the g2o framework (Kümmerle et al., 2011) as back-end in order to model and optimize the graph.

The result of the SLAM are the aligned poses of the robot and their associated LiDAR scans. As a next step the scans are projected into map formats in order to fulfill the requirements of the planning and the internal simulation. The planning needs to distinguish

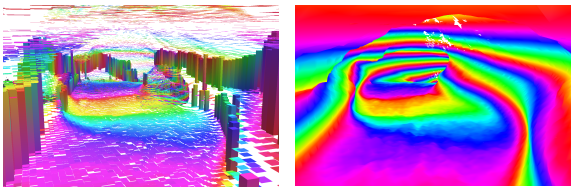

Figure 3: Left: Multi-Level Surface map of a section of the cave with a cell size of 10 cm. Right: Polygon mesh of the same scene. The color indicates the change in altitude, one meter equals one color cycle.

between traversable and non-traversable regions, requires fast access to the local height information and the ability to represent multiple levels. While the internal simulation requires a very accurate representation of the surfaces.

Fig. 3 shows the two map types that are created on request of the path planning and the internal simulation. The planning uses a Multi-Level Surface (MLS) (Triebel et al., 2006) map since it allows to represent multiple levels while accurately encoding height information and uncertainty. It is a 2D grid managing a list of entries providing height, occupancy and uncertainty information for each cell.

In order to create an accurate representation of the surface of the environment for the simulation we extract a polygon mesh from an intermediate map format. The intermediate map format is a voxel grid holding the estimated truncated signed distance to the closest surface and uncertainty in each cell. Modeling truncated signed distance functions (TSDF) (Curless and Levoy, 1996) with the goal of accurate surface reconstruction have been recently used especially in the context of RBGD-camera based SLAM (Newcombe et al., 2011). We show that it can also be applied successfully on LiDAR based SLAM. Each measurement is ray-traced on the line from the sensor origin to the measurement in the range $[-\delta, +\delta]$ around the measurement (δ is the truncation parameter). The CPU based ray tracing is implemented based on the work from (Amanatides et al., 1987). In order to extract the surface from the TSDF volume we use the Marching Cubes algorithm (Lorensen and Cline, 1987).

The generation of those maps from the LiDAR measurements is expensive and not real time capable, therefore they are created on demand by the Internal Simulator. Usually, after the robot has reached the goal position and a new trajectory needs to be planned and evaluated.

2.2 Path Planning

Caves are complex and unpredictable environments that may contain multiple overlapping levels. We approach path planning in such environments by developing a robust algorithm able to cope with multiple 2D levels embedded in a 3D world. Our multi level path planner assumes that the target scenario does not incorporate dynamic obstacles. A reasonable assumption in exploration of extraterrestrial caves.

Path planning in unstructured environments has been thoroughly explored and several solutions have been proposed, e. g., (Daily et al., 1988; Lacroix et al., 2002; Howard and Kelly, 2007; Rekleitis et al., 2013). However, those solution are in general limited to 2D or 2.5D planning and are not suitable for multi path level planning.

Multi level solutions have been proposed in (Kümmerle et al., 2009) and in (B. Rusu et al., 2009). The solution of (Kümmerle et al., 2009) is probably the closest to our implementation. Their solution is also based on MLS maps and uses motion primitives. However they employ a two-steps planning approach where the first step returns a coarse result that is improved by a local planning step, whereas we implemented a one-step solution that yields good results.

In order to plan efficiently, the MLS map provided by the SLAM is converted into a traversability map (TravMap). Our TravMap encodes knowledge about the local traversability using four different patch types: *traversable*, *obstacle*, *unknown* and *explorable*.

A patch is marked traversable if enough support exists in the region for the robot to stand on and there are no obstacles that would hinder the robots traversal. Thus to asses if a patch is traversable, first a surface analysis is performed and second an obstacle check.

In the surface analysis the overall slope of the support plane must not exceed a predefined slope limit and there must not exist steps within the plane that exceed the maximum step height of the robot. If these two requirements are met, the patch is initially considered traversable and obstacle check is performed.

A 3D obstacle check is performed against the MLS using a robot model-based bounding box which ignores the orientation of the system. Thus, patches where the robot won't collide with obstacles when standing in at least one orientation are marked as *traversable*. This approach pursues to find any possible path on the TravMap, by marking as *obstacle* patches only those that are guaranteed to be non-traversable in all robot orientations.

The obstacle check improves performance during the posterior planning steps by performing and initial prune of the search space. Nevertheless, during path planning a more detailed obstacle check is done that incorporates the orientation of the robot.

The local support plane is calculated using

RANSAC (Fischler and Bolles, 1981) plane fitting. Patches are marked as *unknown* in case insufficient data is available to find such a plane (i. e., less than 5 inliers support the plane). Such places usually indicate a lack of data in the map and are natural targets for further exploration. However since critical knowledge is missing in order to assess the traversability of unknown patches, they cannot be the target of a planning process. Therefore, we select traversable patches nearby and mark them *explorable*. The robot should be able to attain more information of the environment by driving onto these patches.

Generating the TravMap is a computationally expensive process that was not compatible with stop-free navigation on our system. Thus, it is performed as less as possible, i. e., only when the robot has reached a goal position while waiting for the next target pose. Due to the static nature of the target environment map re-generation of the TravMap is in our case seldom needed.

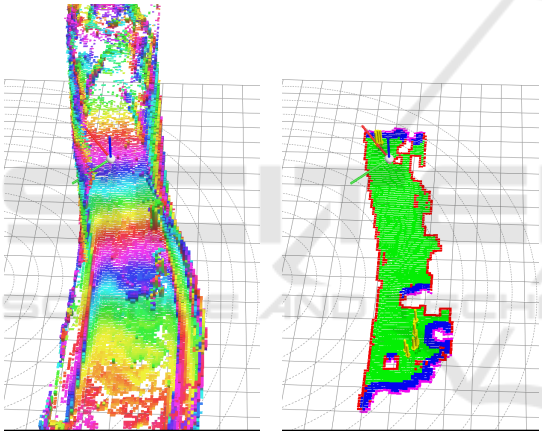

(a) MLS map (b) Traversability map

Figure 4: For exploration and path planning, the Traversabilty Map (b) is generated from the Multi-Level Surface map (a). The coordinates axis describe the current pose of the robot, the background grid has a resolution of 1 m, the resolution of the MLS and the traversability map are 0.1 m. In (b): Green cells represent *traversable* surfaces, red ones *obstacles*, magenta are *unknown* and blue are *explorable* areas. Yellow arrows mark the target candidates for the path planning.

An MLS map and the TravMap that was generated from it are presented in Fig. 4. The map is created by growing from the current robot position. Expansion stops at patches marked as unknown or border, resulting in a 3D representation of all the places that the robot can reach from its current position. Each patch in the map is linked to its neighbors. Thus, it is equivalent to a double connected graph structure that can be searched efficiently for traversable paths.

Path planning is done using SBPL (Cohen et al., 2010; Likhachev et al.,) and the ARA* algorithm (Likhachev et al., 2004). ARA* was chosen due to it's anytime characteristics. It can provide a suboptimal solution quickly and refine it until an optimal solution is found.

In the TravMap, x and y are the coordinates of the patch the robot is standing on and z is the patches height. The state space is discretized and consists of (x, y, z, θ) where x, y and θ are discretized while z remains continuous.

To keep the number of possible state transitions low, two-dimensional spline based *motion primitives* are used to model the robot motions. For distance calculation the primitives are projected onto the 3D surface the robot is driving on. Because the primitives are distorted when projected on a non-flat surface, the final trajectory may contain motions that slightly deviate from the motion primitives.

The time it would take the robot to follow the shortest path on the TravMap is used as heuristic. The cost function consists of the actual time it would take the robot to follow the selected motion primitive as projected onto the 3D surface. Optionally, a term representing the closeness to obstacles can be factored in to favor trajectories that stay well clear of obstacles. The robot's forward, backward and turning speeds can be configured separately and are used to calculate the travel time.

While searching, only collision free motion primitives are considered. To achieve this, a 3D bounding box check against the MLS is computed for every discretized pose that can occur on a given primitive. These checks are the most CPU intensive part of the path planning algorithm. Thus, the overall performance depends largely on the number of motion primitives that need to be checked at each step. However, the obstacle checks can be parallelized, i. e., for a given state all possible successors can be found at the same time as long as enough processing time is available. For this reason, we are able to use a very detailed set of motion primitives and yield good results without any further optimization.

2.3 Internal Simulator

The internal simulation has in this context the task of predicting the probability of a path traverse execution to be successful. Ideally, the accuracy of the prediction is well known. This accuracy is dependent of many factors: Some can be grouped into biases from the simulation (e.g. wrong surface friction estimation, errors in the robot model), others related to the path's complexity (e.g. length, curves, orientation changes) and others due to a certain level of intrisic indetermin-

ism in the simulated and in the real execution.

The internal simulator incorporates running clones of the components from which the results we intend to validate and of the ones they depend on, except for the sensor drivers. The sensor drivers are replaced in this copy of the components network by modules that produce analog data based on the robotics physics engine, or in the case of the cameras, by the graphical engine used to render it. In this case, the cloned components are the path planning, the execution layer and all subcomponents on which they depend, except for the SLAM which is connected to both the original components and their clones. Nevertheless, the SLAM has a different role in the internal simulator: It provides the surfaces of the environment. The surfaces are required to compute physical interactions with the robot model. SLAM is not used for localization of the cloned components interacting with the simulated environment and it does not maintain any environment representation based on simulated sensor data.

The cloned components and their interactions take place on the same Robotic Control Operating System than the original components and on-board the system. Thus, their interactions and resulting behavior are highly similar. We consider this an important feature because delays in the communication layer between components can have consequences more difficult to predict outside the system itself.

The validation process of a goal position in the internal simulation is the following: (1) The internal simulation requests to the SLAM module a polygon mesh. The mesh is generated from the aligned point cloud that SLAM maintains and it has a resolution of 5 cm. (2) With the mesh, the simulated environment, in which the physical model of the robot is also placed according to its estimated pose, is updated. (3) A TravMap is generated based on the MLS map of the environment which is also provided by the SLAM. (4) The path planning uses the TravMap to plan a path. (5) The plan execution is simulated on-board. (6) If the target is reached, the goal pose is considered validated and the goal pose is passed to the executive layer. Otherwise, feedback is provided to the Exploration Module, so that another target pose is selected.

The internal simulation is complex and requires high computational costs. Thus, it must be carefully decided in which situations it should be used. Furthermore, depending on the hardware available, its integration might be unfeasible or only possible after a careful adaptation of the different process priorities. In fact, this is the first application know to the authors where the robotics simulator runs on-board along with the rest of the components. A requirement for scenarios where access to external computational resources is not possible like the one targeted.

In order to minimize the computational costs and increase the reliability of the approach, a new environment representation library (Hidalgo Carrió et al., 2016) has been developed. The library lies both at the core of SLAM and the Internal Simulation. Using the same environment representation in both components has at least two advantages: (1) It reduces the number of dependencies of the software and (2) minimizes the conversions between representation models. To the best of the authors knowledge, this is the first case of a robotic setup in which the simulated scenes are generated on-board based on the environment representation that the system itself constructs, instead of using pre-designed simulated scenes with little or no change.

Another tool shared by different components is the Flexible Collision Library from (Lee et al., 2017), which is used in the collision check of the path planning and to determine the collisions between the robot model and the simulated surfaces.

2.4 Exploration

Relying on the previously described components, the following exploration behavior has been implemented and tested: First, each *explorable* patch on the map is evaluated based on its proximity to the current robot pose, number of unexplored patches nearby and proximity to a specified target position.

A path is planned to the most promising patch. If no path could be found or its simulation execution determines a failure, the next candidates are analyzed until a safe path is found.

Once a path has been found, the robot starts following the Trajectory and once the target position is reached, the current MLS is updated and a new TravMap map is generated. The process repeats until the desired area has been explored or another criteria (e. g., a time limit or low battery condition) is fulfilled, at which point the robot returns to its starting pose. The return is relevant for cave scenarios because the system needs to recharge and establish communication after the exploration.

Terrain conditions inside the cave are unknown and most likely complex. The robot might get stuck, slip or skid at random locations. Thus the robot might deviate from the planned trajectory while moving. To avoid leaving the traversable map and running into obstacles we continuously monitor the current robot position and stop the motion if the robot is about to leave the traversable part of the map. If this happens the maps are updated and the exploration process re-

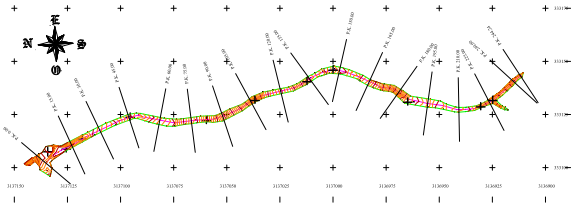

Figure 5: A map of the cave with some geo-referenced points on it (crosses). These points were marked with magenta spheres when taking the data logs in order to use them as ground truth to estimate the accuracy of our localization and mapping. Image: Courtesy of Geodata air S.A.

peats.

In certain situations, borders of the currently explored map cannot be distinguished from actual down-hill cliffs, e. g., if the LiDAR is not able to see any surface after the cliff. This would result in the exploration strategy repeatedly trying to explore already visited places. To avoid this, we implemented a simple coverage map, which accumulates the areas around the robot positions. Patches which are covered by this map, will not be considered as candidates for exploration.

3 RESULTS

In this section we summarize experiments performed to test the different modules and its interactions in an analog scenario to a Martian or Lunar lava tube. The experiments were conducted with the Asguard V4 rover in a 240 meter long section of the *Cueva del Viento* lava tube in November of 2017. The covered section starts at the entrance *Breveritas* and goes to the South. In Fig. 5 a cartographic representation of the cave produced by a topographic company is shown. It represents the different elevations and some geo-referenced positions which were used as ground truth.

The rover is equipped with a Xsens IMU, a Velodyne HDL-32E LiDAR and two cameras with super fish eye lenses. Each camera has a horizontal opening angle of 220°, fully covering 360° around the rover.

3.1 Cave Mapping

In this section we show that the accuracy of the pose graph of our SLAM solution is within a mean position difference of 0.4 m to the ground truth.

In order to evaluate the accuracy of our SLAM solution eleven globally referenced landmarks in the 240 m long subsection of the lava tube were used as ground truth. Prior to our experiments those survey markers (≈ 5 mm metal pins) had been located within

Figure 6: Shows an artificial landmark (magenta colored sphere) placed on a position for which ground truth information was available. The Apriltag in the background was used to distinguish between different landmarks.

an independent geodetic survey. The ground truth positions are associated with an uncertainty of 0.05 m.

In order to later identify the landmarks in the camera images, we placed magenta colored spheres with a diameter of 8 cm on top of the survey markers. The landmarks were not integrated in the SLAM to improve the positioning or map construction, we only compared the expected position of the landmarks in the SLAM with their known ground truth positions.

The positions of the spheres in the camera images were detected by applying a HSV (Hue, Saturation, Value) based color segmentation followed by a circle Hough Transformation. Since the only source of light inside of the cave were the lights of the rover, the detection was prone to strongly changing light conditions, reflections on the surface of the spheres and outliers (Fig. 6). Therefore, especially the detected size of the sphere in the image needed to be associated with a higher uncertainty.

For collecting this data set the rover was first manually driven, from a starting point above one of the landmarks, 240 m into the cave and then back to the starting point. Fig. 7 shows the trajectory (blue line) of the robot during the mission in North/East and North/Altitude direction. The starting point is at the origin of the local coordinate frame. The red crosses show the known positions of the landmarks in the local frame and the green crosses show their expected positions in the SLAM.

Since the ground truth information is only available when spheres are detected in the camera images, the difference to the ground truth can only be observed for the corresponding robot poses at those times. We assume that the error grows approximately linear during the time between observing different landmarks.

To compute the mean position difference we applied a bundle adjustment of the expected positions of the landmarks to the ground truth. As a result the

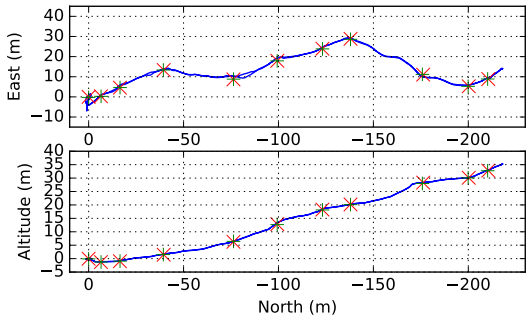

Figure 7: Top: North-East trajectory of the robot. Bottom: North-Altitude trajectory of the robot. The red crosses show the globally referenced landmarks used as ground truth and the green crosses show the mean of their expected position.

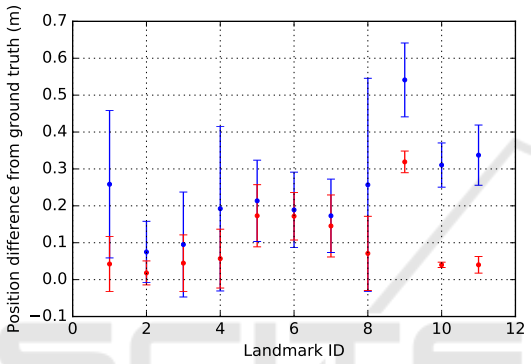

Figure 8: Blue: Position difference from ground truth and associated standard deviation for each landmark. Red: Difference in altitude from ground truth and associated standard deviation.

mean position difference to the ground truth is within 0.4 m over the whole trajectory. The mean difference in altitude direction is within 0.17 m, due to modeling the IMU based inclination constraints in the SLAM (Eq. 6).

Fig. 8 shows the mean position difference to the ground truth and associated standard deviation for each single landmark. The landmarks are arranged

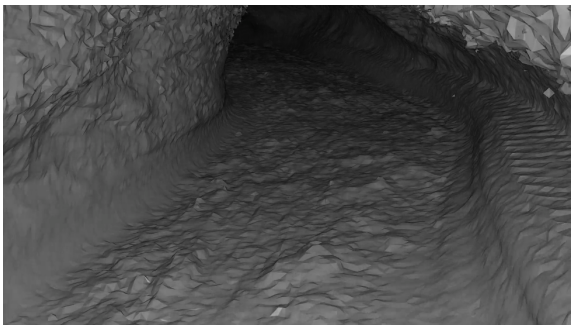

Figure 9: Polygon mesh of the cave, generated from a TSDF voxel grid with a resolution of 5 cm. The cave diameter at this section is approx. 4 m.

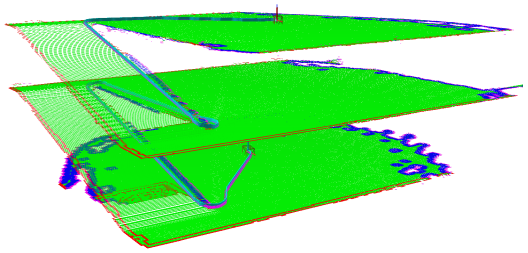

Figure 10: Path planning test in a simulated oversized parking garage.

from ID 1 at the origin of the mission up to ID 11 at the furthest area inside the cave. The diversity and magnitude of deviations is due to the challenges in the sphere detection. The amount of measurements to compute the means and standard deviations variates between 7 (ID 6) and 41 (ID 5, ID 11) with a mean of 24 observations per landmark. It can be seen that the position difference is higher in the North/East direction since we are able to reduce the error in altitude direction by modeling the inclination constraints.

Fig. 9 shows the polygon mesh generated from the LiDAR measurements projected into a TSDF voxel grid with a resolution of 5 cm.

3.2 Path Planning

We tested several simulated as well as real scenarios to benchmark the path planner. All tests were done on an Intel Core i7-6700 using all available cores. The set of motion primitives used for all tests consists of 850 primitives. In order to reduce the friction of the wheels and the chances of damage on the rough lava tube surfaces, point turns where not included in the motion primitives.

The multi level planning capability is first shown in a simulated parking garage as the accessible part of the cave on Tenerife does not have multiple levels. The TravMap of the garage consists of 128478 patches covering 1284.78 m^2 at a grid resolution of 0.1 m while the TravMap of the cave consists of 59083 patches covering 590.83 m^2.

Planning of a trajectory from lowest to the highest level of the garage as seen in Fig. 10 took 80.39 s of CPU time or 40.13 s of real time. Fig. 11 represents a standard case: planning of a trajectory of 43.48 m length in the cave. Planning took 426.78 s of CPU time and 65.88 s of real time. A more complex case is shown in Fig. 12. Here the impact of lots of obstacles can be observed. Two trajectories were computed, the optimal solution took 2276.87 s of CPU time or 343.6 s of real time while a suboptimal solution was found in 102.21 s of CPU time or

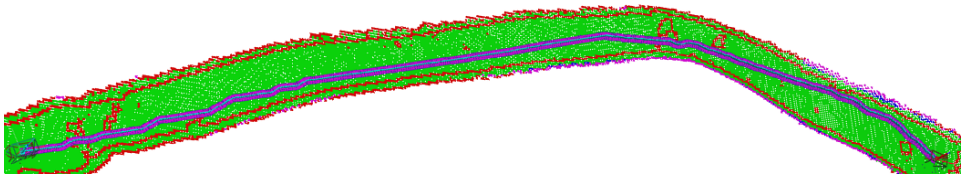

Figure 11: Planning a trajectory of 43.48m length in a cave.

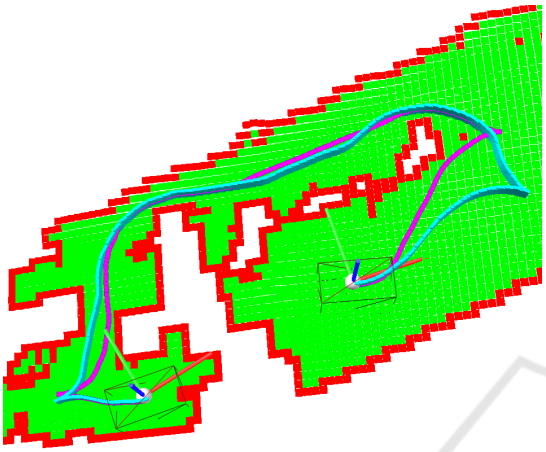

Figure 12: Path planning test in the cave with a lot of obstacles. The cyan trajectory is optimal, the magenta trajectory is a suboptimal solution. The wireframe boxes show the robot's bounding box. The coordinate systems show the start and end pose of the robot.

27.365 s of real time. The trajectories are 12.12 m and 11.62 m long respectively. This case especially shows the value of using the ARA* algorithm, which can be parametrized whether to decide to wait for the optimal path or just use a suboptimal one to get on with the task as soon as possible.

3.3 Internal Simulation

Among all the navigation experiments performed in the cave, we have selected one trajectory to analyze the accuracy of the internal simulation. The initial and target position of the robot and the traversed paths are shown in Fig. 13, along with the correspondent visualization of the generated simulation. The path has two sections, the first one is a straight trajectory and the second a curve started after a direction change. Our path planning has been configured to avoid point turns in the rough surfaces of the lava tube. In other surfaces, a point turn and a straight trajectory would have been more efficient.

We analyzed the distance between the most accurate estimation of the position that was available for the robot and the positions in the simulated execution. The poses from the simulation are directly provided by the physical engine. While the estimation of the real poses of robot were obtained offline after an expensive ICP-based pose graph relaxation on the collected pointclouds.

In order to analyze how different the real path and the simulated path are, a distance function is defined. The distance function must take into account the positions where the robot went as well as the time relative to the beginning of the path traverse. We compare the positions of the robot and the simulated robot at the same time stamps relative to the time stamp when the movement starts.

Fig. 14 shows the distances measured between poses at same relative time stamps since the beginning of the motion. The SLAM-based pose estimation updates are less frequent than the simulation pose updates. Thus, in order to apply the error estimation function, first a sub-sampling of the pose samples of the simulation was done.

In Fig. 15 the error is shown with respect to time. The average of the Root Mean Squared Error (RMSE) between simulated and real poses was 0.419 m for this path execution. During the first section of the trajectory execution, positions do not accumulate a large error, but the error increases during the turn. Finally, when both reach the end of the trajectory the error decreases again. One of the main causes of the error in the second section of the trajectory is that the robot reaches the goal position already at 14th second in simulation while the real one takes 4 seconds more. The delay in the real execution is caused by a lack of accuracy in the surface friction model as well as in the robot model (e.g. simulated motors).

Another insight that we found interesting when analyzing the results is shown in Fig. 16. Due to the lower frequency at which ICP can run on the system with respect to the wheel odometry, errors in the position estimation generated by the wheel odometry can be identified as spikes in the on-board pose estimation. We have identified the possibility of correcting online the pose estimation by using the poses from the internal simulated path execution. Especially, if higher accuracy is achieved through better parametrization and modeling of the simulation.

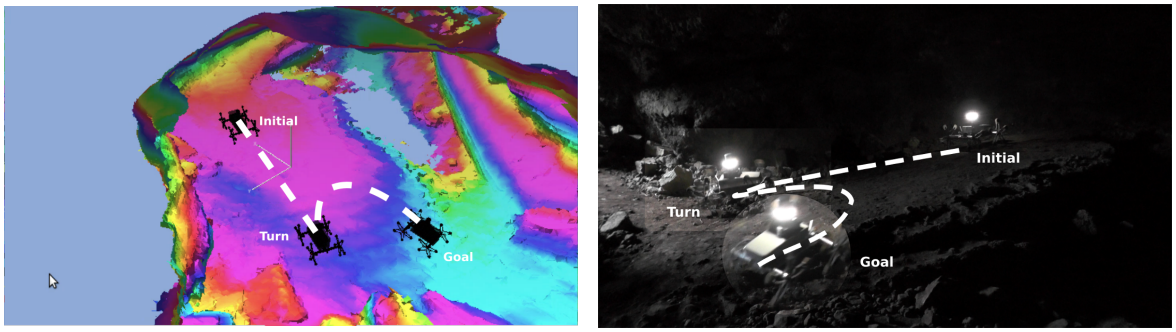

(a) Internally simulated trajectory execution (b) Trajectory performed by the real robot

Figure 13: The internal simulation (a) is produced from sensor data taken by the real robot. It can run on-board the system and has been used for path execution validation before real execution (b) is done.

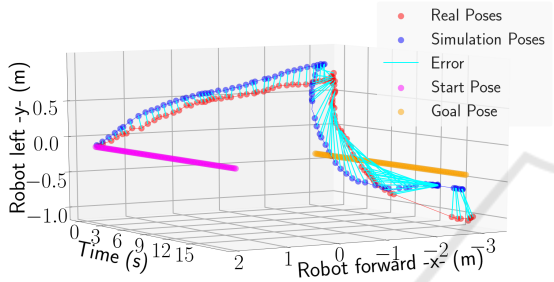

Figure 14: Measurement of the error between the two path executions, points from the simulation path are sub-sampled according to the time stamps at which the poses of the real execution are available.

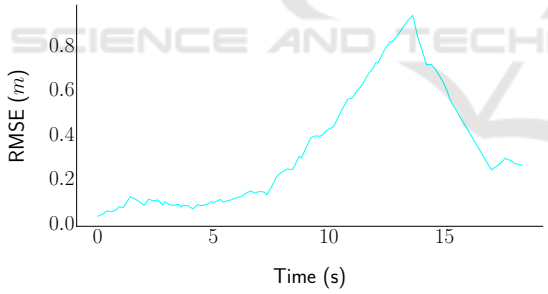

Figure 15: Error between real position estimation and simulated position during internal simulation and posterior execution of the trajectory. Error increases during a turn and because the final position is reached faster in the simulation.

3.4 Exploration

In Fig. 17 we show an example how the cave gets explored successively. Targets near the current robot pose are preferred, as long as they are expected to result in newly observed areas. We did not put much effort into refining or optimizing the exploration behavior, as our ad-hoc implementation gave sufficient results for our purposes.

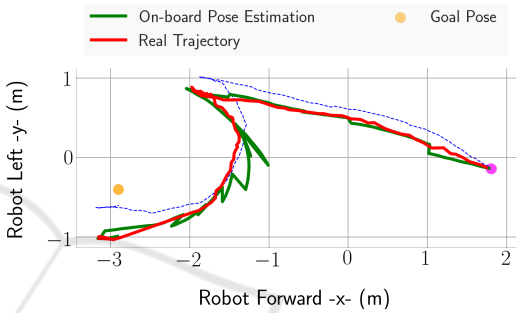

Figure 16: The poses of the executed trajectory in simulation and real execution are displayed together. In this case, the simulation predicts a successful path execution.

4 CONCLUSIONS

A novel approach for safe autonomous exploration of lava tubes in a space scenario composed of SLAM, Internal Simulation, Path Planning and Exploration modules has been described. This methodology is based on a graph-SLAM. Models with associated uncertainty for both planning (the MLS map) and Internal Simulation (an accurate polygon mesh) are generated on demand.

The experiment performed in the lava tube shows an accuracy of position in average of 0.6 m. The ground truth was calculated by identifying georeferenced markers and performing bundle adjustment of the collected sensor data with the correct position of the markers.

The proposed Path Planning uses specific robot motion primitives to efficiently search in the space of solutions offered by the graph of connected traversable patches which was generated from the MLS map. The planner is different from previous approaches since it only uses one path for the complete traverse achieving successful results and it is able to find solutions in environments with multi-

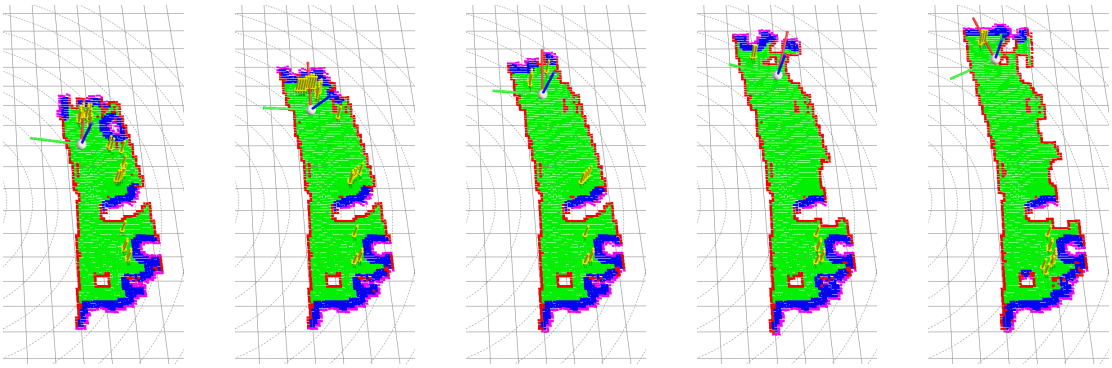

Figure 17: Sequence of traversability maps, showing the exploration behavior

ple unstructured traversable surfaces. In the cave experiments our path planning was able to provide traversable paths of 12.12 m in highly unstructured areas in 27.365 s. In areas of the tube with less obstacles, planning of a long trajectory is achieved in 65.88 s for 43.48 m.

The first on-board robotic simulator which relies on the environment representation of the robot to update the simulated environment was presented. It is used to accurately replicate the path planning and execution modules of the robot for validation of potential goal poses. In the experimental section, a procedure to analyze the error in the trajectory execution was presented. The methodology is useful to better estimate the prediction horizon in which the simulation can be considered realistic. While error in the prediction of straight trajectories is low, turns are more difficult to predict accurately. Further executions of the simulated and the real path executions are envisioned to provide more statistical significant results in the future. It has as well been identified that the results of the simulated executions could be useful as a correcting vector for the pose estimation.

The exploration behavior allows for the mapping of unknown regions. It selects traversable goal poses for which navigation from the current pose has been predicted as successful by the internal simulator.

ACKNOWLEDGMENT

The presented work was developed in the Entern project (grant No. 50RA1406, 50RA1407) which is funded by the German Federal Ministry of Economics and Technology (BMWi).

We greatly acknowledge *Museos de Tenerife and Cueva del Viento* for giving us access to the lava tube and for providing us with local support in many ways.

REFERENCES

Amanatides, J., Woo, A., et al. (1987). A fast voxel traversal algorithm for ray tracing. In *Eurographics*, volume 87, pages 3–10.

B. Rusu, R., Sundaresan, A., Morisset, B., Hauser, K., Agrawal, M., Latombe, J., and Beetz, M. (2009). Leaving flatland: Efficient real-time three-dimensional perception and motion planning. *J. Field Robot.*, 26(10):841–862.

Chella, A. and Macaluso, I. (2009). The perception loop in CiceRobot, a museum guide robot. *Neurocomputing*, 72(4-6):760–766.

Cohen, B. J., Chitta, S., and Likhachev, M. (2010). Search-based planning for manipulation with motion primitives. In *2010 IEEE International Conference on Robotics and Automation*, pages 2902–2908.

Curless, B. and Levoy, M. (1996). A volumetric method for building complex models from range images. In *Proceedings of the 23rd annual conference on Computer graphics and interactive techniques*, pages 303–312. ACM.

Daga, A. W., Allen, C., Battler, M. M., Burke, J. D., Crawford, I. A., Léveillé, R. J., Simon, S. B., and Tan, L. T. (2009). Lunar and martian lava tube exploration as part of an overall scientific survey. In *Annual Meeting of the Lunar Exploration Analysis Group*, volume 1515, page 15.

Daily, M., Harris, J., Keirsey, D., Olin, D., Payton, D., Reiser, K., Rosenblatt, J., Tseng, D., and Wong, V. (1988). Autonomous cross-country navigation with the ALV. In *[No source information available]*, volume 2, pages 718 – 726.

Domínguez, R., Schwendner, J., and Kirchner, F. (2015). On-board simulator for autonomy enhancement in robotic space missions. In *In Symposium on Advanced Space Technologies in Robotics and Automation (ASTRA)*.

Fischler, M. A. and Bolles, R. C. (1981). Random sample consensus: A paradigm for model fitting with applications to image analysis and automated cartography. *Commun. ACM*, 24(6):381–395.

Hertzberg, C., Wagner, R., Frese, U., and Schröder, L. (2013). Integrating generic sensor fusion algorithms

with sound state representations through encapsulation of manifolds. *Information Fusion*, 14(1):57–77.

Hesslow, G. (2012). The current status of the simulation theory of cognition. *Brain research*, 1428:71–9.

Hidalgo Carrió, J., Arnold, S., Böckmann, A., Born, A., Domínguez, R., Hennes, D., Hertzberg, C., Machowinski, J., Schwendner, J., Yoo, Y., and Kirchner, F. (2016). EnviRe - environment representation for long-term autonomy.

Howard, T. M. and Kelly, A. (2007). Optimal rough terrain trajectory generation for wheeled mobile robots. *The International Journal of Robotics Research*, 26(2):141–166.

Kümmerle, R., Grisetti, G., Strasdat, H., Konolige, K., and Burgard, W. (2011). g^2o: A general framework for graph optimization. In *Robotics and Automation (ICRA), 2011 IEEE International Conference on*, pages 3607–3613. IEEE.

Kümmerle, R., Hahnel, D., Dolgov, D., Thrun, S., and Burgard, W. (2009). Autonomous driving in a multi-level parking structure. In *2009 IEEE International Conference on Robotics and Automation*, pages 3395–3400.

Lacroix, S., Mallet, A., Bonnafous, D., Bauzil, G., Fleury, S., Herrb, M., and Chatila, R. (2002). Autonomous rover navigation on unknown terrains: Functions and integration. *The International Journal of Robotics Research*, 21(10-11):917–942.

Lee, J. et al. (2017). Flexible collision library. https://github.com/flexible-collision-library/fcl.

Likhachev, M. et al. Search-based planning lab. http://www.sbpl.net.

Likhachev, M., Gordon, G. J., and T., S. (2004). ARA*: Anytime A* with provable bounds on sub-optimality. In Thrun, S., Saul, L. K., and Schölkopf, B., editors, *Advances in Neural Information Processing Systems 16*, pages 767–774. MIT Press.

Lorensen, W. E. and Cline, H. E. (1987). Marching cubes: A high resolution 3d surface construction algorithm. In *ACM siggraph computer graphics*, volume 21, pages 163–169. ACM.

Marques, H. G. and Holland, O. (2009). Architectures for functional imagination. *Neurocomputing*, 72(4-6):743–759.

Nesnas, I. A. D., Matthews, J. B., Abad-Manterola, P., Burdick, J. W., Edlund, J. A., Morrison, J. C., Peters, R. D., Tanner, M. M., Miyake, R. N., Solish, B. S., and Anderson, R. C. (2012). Axel and duaxel rovers for the sustainable exploration of extreme terrains. *Journal of Field Robotics*, 29(4):663–685.

Newcombe, R. A., Izadi, S., Hilliges, O., Molyneaux, D., Kim, D., Davison, A. J., Kohi, P., Shotton, J., Hodges, S., and Fitzgibbon, A. (2011). KinectFusion: Real-time dense surface mapping and tracking. In *Mixed and augmented reality (ISMAR), 2011 10th IEEE international symposium on*, pages 127–136. IEEE.

Preston, L., Barber, S., and Grady, M. (2012). Concepts for activities in the field of exploration (cafe). tn2: The cataloge of planetary analogues.

Rekleitis, I., Bedwani, J., Dupuis, E., Lamarche, T., and Allard, P. (2013). Autonomous over-the-horizon navigation using LIDAR data. *Autonomous Robots*, 34(1):1–18.

Rockel, S., Klimentjew, D., Zhang, L., and Zhang, J. (2014). An hyperreality imagination based reasoning and evaluation system (HIRES). In *2014 IEEE International Conference on Robotics and Automation (ICRA)*, pages 5705–5711.

Rockel, S., Konečný, Š.and Stock, S., Hertzberg, J., Pecora, F., and Zhang, J. (2015). Integrating physics-based prediction with semantic plan execution monitoring. In *2015 IEEE/RSJ International Conference on Intelligent Robots and Systems (IROS)*, pages 2883–2888.

Roßmann, J., Guiffo Kaigom, E., Atorf, L., Rast, M., Grinshpun, G., and Schlette, C. (2014). Mental models for intelligent systems: eRobotics enables new approaches to simulation-based AI. *KI - Künstliche Intelligenz*, 28(2):101–110.

Segal, A., Haehnel, D., and Thrun, S. (2009). Generalized-ICP. In *Robotics: Science and Systems*, volume 2, page 435.

Triebel, R., Pfaff, P., and Burgard, W. (2006). Multi-level surface maps for outdoor terrain mapping and loop closing. In *Intelligent Robots and Systems, 2006 IEEE/RSJ International Conference on*, pages 2276–2282. IEEE.

Wynne, J. J. (2016). The scientific importance of caves in our solar system: Highlights of the 2nd international planetary caves conference, Flagstaff, Arizona. *NSS NewS*, page 5.